

Jet-torus interaction revealed by sub-parsec SO absorption in NGC 1052

Satoko SAWADA-SATOH,^{1,2} ^{,*} **Seiji KAMENO**,^{3,4,5} **Nozomu KAWAKATSU**,⁶ **Do-Young BYUN**,^{7,8} **Se-Jin OH**,⁷ **Sang-Sung LEE**,^{7,8} **Duk-Gyoo ROH**,⁷ **Chungsik OH**,⁷ **Jae-Hwan YEOM**,⁷ **Dong-Kyu JUNG**,⁷ **Hyo-Ryoung KIM**,⁷ **Young-Sik KIM**,⁷ and **Sanghyun KIM**⁷

¹Graduate School of Science, Osaka Metropolitan University, 3-3-138 Sugimoto Sumiyoshi-ku, Osaka 558-8585, Japan

²Faculty of Engineering, Fukui University of Technology, 3-6-1 Gakuen, Fukui City, Fukui 910-8505, Japan

³Joint ALMA Observatory, Alonso de órdova 3107 Vitacura, Santiago 763-0355, Chile

⁴National Astronomical Observatory of Japan, 2-21-1 Osawa, Mitaka, Tokyo 181-8588, Japan

⁵Department of Astronomy, School of Science, Graduate University for Advanced Studies (SOKENDAI), Tokyo 181-8588, Japan

⁶National Institute of Technology, Kure College, 2-2-11 Agaminami, Kure, Hiroshima 737-8506, Japan

⁷Korea Astronomy and Space Science Institute, 776 Daedeok-daero, Yuseong, Daejeon 34055, Republic of Korea

⁸University of Science and Technology, 217 Gajeong-ro, Yuseong-gu, Daejeon 34113, Republic of Korea

*E-mail: swdsth@gmail.com

ORCID: 0000-0001-7719-274X, 0000-0002-5158-0063, 0000-0003-2535-5513

Abstract

We report the first $\lambda 2$ -mm very long baseline interferometry (VLBI) observations of the radio galaxy NGC 1052, conducted with the Korean VLBI Network (KVN) using a wide-band recording mode. Leveraging the wide bandwidth covering a velocity range at 2300 km s^{-1} , we successfully detect broad ($> 700 \text{ km s}^{-1}$) multi-component SO $J_N = 3_3 - 2_2$ absorption against the sub-parsec-scale continuum structure. The absorption profile consists of both redshifted and blueshifted components, including a newly identified blueshifted feature at -412 km s^{-1} relative to the systemic velocity. Significant SO absorption is confined to the central components, with no substantial detection toward the outer jet components. This constrains the location of SO gas to a compact region smaller than 0.45 pc in the sub-parsec vicinity of the supermassive black hole (SMBH). Our results support the scenario in which SO molecules are evaporated through shock heating caused by jet-torus interaction. The SO gas clumps are likely driven outward by the jet, with some returning toward the SMBH as inflowing material. Comparison with 321 GHz H₂O masers reveals partial similarities in spatial distribution and radial velocity, suggesting that the jet-torus interaction may also trigger the excitation of H₂O masers.

Keywords: galaxies: active — galaxies: individual (NGC 1052) — galaxies: nuclei — ISM: absorption lines — ISM: jets and outflows

1 Introduction

The properties of circumnuclear media at the centers of galaxies play a crucial role in various phenomena associated with active galactic nuclei (AGNs). It is widely accepted that AGNs are powered by the accretion of circumnuclear gas (Lynden-Bell 1969), which serves as the reservoir fueling the central supermassive black hole (SMBH). Moreover, the circumnuclear medium is a key component of the AGN unification model. A toroidal distribution of gas surrounding the SMBH, commonly referred to as the “torus”, is responsible for obscuration of the broad-line region, thereby naturally explaining the observed dichotomy between type 1 and type 2 Seyfert galaxies (Antonucci 1993; Urry & Padovani 1995). In addition, recent observations of nearby AGN jets using Very Long Baseline Interferometry (VLBI) have revealed that the relativistic jets are highly collimated within the nuclear region (e.g., Asada & Nakamura 2012; Hada et al. 2013). These findings suggest that the circumnuclear medium may play a significant role in collimating jets by exerting pressure. Therefore, detailed investigations into the morphology and kinematics of the circumnuclear gas surrounding the SMBH are essential for advancing our understanding of AGN fueling mechanisms and jet collimation pro-

cesses.

NGC 1052 is a nearby elliptical galaxy with a systemic velocity (V_{sys}) of $1492 \pm 2.6 \text{ km s}^{-1}$ (Kameno et al. 2020) with respect to the local standard of rest (LSR). Its central region hosts a low-luminosity AGN characterized by a low-ionization nuclear emission-line region (LINER) spectrum (e.g., Gabel et al. 2000), as well as a hidden broad line region (BLR) detected in polarized light (Barth et al. 1999). The nucleus is surrounded by a central condensation of ambient gas in multiple phases. Past high-resolution observations have found atomic and molecular absorption lines including H I (Vermeulen et al. 2003), OH (Omar et al. 2002; Impellizzeri et al. 2008), CO, HCN, HCO⁺, SO, SO₂, CS, CN, and H₂O toward the center of NGC 1052 (Liszt & Lucas 2004; Kameno et al. 2020). H₂O megamaser emission has also been mapped in the parsec (pc) scale region using the Very Long Baseline Array (VLBA) at 22 GHz (Claussen et al. 1998; Sawada-Satoh et al. 2008) and the Atacama Large Millimeter/submillimeter Array (ALMA) at 321 GHz (Kameno et al. 2023b, 2024). Multi-frequency VLBI images have also shown a central condensation of ionized gas surrounding the SMBH (Kameno et al. 2001, 2003). This multiphase gas condensation has been interpreted as a circumnuclear torus comprising several

layers with temperatures ranging from 10^2 to 10^4 K (Kameno et al. 2005; Sawada-Satoh et al. 2008). Hot (10^4 K) ionized gas resides on the inner surface layer and obscures the base of the nuclear jet, producing the emission gap between the eastern approaching and western receding jets at frequencies of ≤ 22 GHz due to free-free absorption (FFA) by ionized gas (Kameno et al. 2001, 2003; Vermeulen et al. 2003; Kadler et al. 2004; Sawada-Satoh et al. 2008). A nuclear component is obscured within this emission gap below 43 GHz, but becomes visible at 43 GHz and higher frequency bands (Kadler et al. 2004; Sawada-Satoh et al. 2008; Bacsko et al. 2016; Sawada-Satoh et al. 2016, 2019). Adjacent to the ionized layer, a warm (~ 400 K) molecular layer contains excited H₂O molecules with an inverted population distribution, that produces the 22 GHz maser emission. Cooler molecular gas (< 400 K) lies at outer radii of the torus, and molecular absorption lines can be detected on the background continuum component. The gas in the molecular layers exhibits redshifted spectral lines (Sawada-Satoh et al. 2008; Kameno et al. 2023a) indicating infall motion toward the SMBH. ALMA observations of molecular absorption lines by Kameno et al. (2020) proposed a thick torus geometry with a radius of 2.4 ± 1.3 pc and a height-to-radius ratio of 0.7 ± 0.3 . Modeling studies indicate that the torus models with a steep density gradient along the jet axis can simultaneously reproduce the sub-parsec (sub-pc) scale distribution of FFA opacity and the broadband X-ray spectra (Baloković et al. 2021).

NGC 1052 is also known to host a prominent double-sided radio jet ranging from sub-pc to kilo-pc scales along the east-west direction (e.g., Jones et al. 1984; Wrobel 1984; Kellermann et al. 1998). The jet maintains a well-collimated structure within a distance of 10^4 Schwarzschild radii from the SMBH (Nakahara et al. 2020; Bacsko et al. 2022), whose mass is estimated to be $10^{8.19} M_\odot$ (Woo & Urry 2002). It has been suggested that the nuclear jet interacts with dense gas clumps embedded in a geometrically thick torus, and such jet-torus interaction can lead to the jet collimation on sub-pc scale (e.g., Fromm et al. 2019). ALMA observations of the 321 GHz H₂O maser emission in NGC 1052 further indicate that such jet-torus interactions can also affect the excitation of the H₂O masers (Kameno et al. 2023b, 2024). Observations of sulfur-bearing species such as SO, SO₂ and CS are particularly valuable for probing the jet-torus interaction, as these species are considered to be reliable shock tracers (e.g., Pineau des Forets et al. 1993).

ALMA studies of sulfur-bearing molecular absorption have revealed a warm (344 ± 43 K) environment in the torus, derived from submillimeter SO absorption lines at rest frequencies (ν_{rest}) of ≥ 240 GHz (Kameno et al. 2020, 2023a). This temperature is consistent with the presence of 22 GHz H₂O maser emission, and the detection of vibrationally excited HCN and HCO⁺ absorption lines, both of which are associated with the torus. Kameno et al. (2023a) suggested that the jet-torus interaction is responsible for shock heating of gas and dust in the inner regions of the torus, where SO molecules are likely to desorb from the icy mantles of dust grains. Moreover, the observations of millimeter-wave SO absorption lines at rest frequencies ν_{rest} of ≤ 129 GHz reveal complex and asymmetric line profiles, including a redshifted peak around $V_{\text{sys}} + 160$ km s⁻¹, a sharp redward edge around $V_{\text{sys}} + 200$ km s⁻¹, and a shallow blueward slope down to $V_{\text{sys}} - 200$ km s⁻¹. These features point to a dynamic and inhomogeneous medium comprising multiple kinematic components and varying line-of-sight geometries relative to the background continuum. To gain deeper insight into the jet-torus interaction, it is crucial to spatially resolve the millimeter SO absorption and to precisely determine

both the spatial distribution and kinematic properties of the SO gas through high-resolution observations.

Following the ALMA studies that detected jet-torus interaction by Kameno et al. (2023a), we carried out VLBI observations of the SO $J_N = 3_3 - 2_2$ absorption line ($\nu_{\text{rest}} = 129.13892$ GHz) in the sub-pc region of NGC 1052 using the Korean VLBI Network (KVN) in wideband mode. The SO $J_N = 3_3 - 2_2$ absorption line was previously detected with a peak optical depth of 0.0214 using ALMA (Kameno et al. 2023a). We adopt a redshift of $z = 0.005$ for NGC 1052, such that one milliarcsecond (mas) corresponds to 0.095 pc in the galaxy. The radial velocities are hereafter expressed relative to the LSR.

2 Observations and data reduction

KVN Observations of NGC 1052 were conducted on 2020 January 4 and 5, yielding a total on-source time of 14.5 hr. In addition to NGC 1052, the bright continuum sources 3C 84, NRAO 150 and J0423–0120 were observed for 6 minutes every 1 hr for fringe finding and calibration. To improve the sensitivity for the $\lambda 2$ mm SO $J_N = 3_3 - 2_2$ absorption line observations, simultaneous dual-frequency data at 21.5 GHz ($\lambda 1.3$ cm) and 129 GHz ($\lambda 2$ mm) were recorded using the KVN multi-frequency receiving system (Han et al. 2008, 2013) and the new high-speed sampler OCTAD (Oyama et al. 2016, 2024). The data were acquired at a rate of 16 Gbps with four spectral windows (SWs), each covering 1024 MHz with dual circular polarization.

Two of four SWs were assigned to left- and right-hand circular polarization (LHCP and RHCP) at 129 GHz for the target frequency band. The remaining two SWs were set to LHCP and RHCP at 21.5 GHz for the phase referencing. The velocity coverage of one SW was 2300 km s⁻¹ at 129 GHz. Correlation was carried out with the DiFX software correlator (Deller et al. 2007) at the Korea-Japan Correlation Center (Lee et al. (2015); see also KVN Status Report¹), outputting two parallel-hand polarization (LL and RR) visibility products. The parallel-hand polarization data were later averaged into the total intensity data during post-correlation processing.

Post-correlation processing, including calibration, data editing and imaging, was performed using the NRAO Astronomical Image Processing System (AIPS; Greisen 2003). Since the KVN antennas have altitude-azimuth mounts, parallactic angle correction was applied at the outset. A priori amplitude calibration was conducted using elevation-dependent gain curves and system temperature measurements recorded at each station during the observations. Corrections for Doppler-shifted velocities in the SO absorption line, caused by Earth's motion, were also applied. Complex bandpass calibration for each circular polarization hand was performed using 3C 84, NRAO 150 and J0423–0120. The amplitude and phase components of the bandpass solutions were derived from auto-correlation and cross-correlation data, respectively (e.g., Kemball et al. 1995). Prior to applying the bandpass correction, residual delays and rates on the bandpass calibrators were removed to ensure coherent visibility phases across frequency and time. We then derived the complex bandpass solutions by coherently averaging the data over time. The resulting bandpass solutions were applied to the data, yielding residual amplitude ripples corresponding to a fractional amplitude error of less than 2 %. To mitigate rapid phase fluctuations at 129 GHz caused by atmospheric turbulence, we employed the frequency phase transfer method, transfer-

¹ https://radio.kasi.re.kr/status_report/files/KVN_status_report_2025.pdf

ring phase solutions from the lower-frequency data (21.5 GHz) to the higher-frequency data (129 GHz) by scaling according to their frequency ratio (Middelberg et al. 2005; Rioja & Dodson 2011).

We generated continuum data by averaging all channels, and a spectral cube with a frequency interval of 16 MHz. Fringe-fitting and self-calibration solutions derived from the continuum data were applied to the cube. The visibility data were imaged without *uv*-taper using natural weighting. The resulting synthesized beam size is 0.88×0.73 mas, corresponding to 0.084×0.069 pc in NGC 1052. Continuum emission was identified and subtracted from the spectral cube by fitting a polynomial to line-free channels.

Finally, optical depth images of SO absorption were derived by combining the continuum map and the line channel maps. We clipped out image pixels with intensities below $7.1 \text{ mJy beam}^{-1}$ ($< 5 \sigma$) in the continuum map due to poor signal-to-noise ratio in the optical depth at positions with weak continuum emission. We note that the SO $J_N = 3_3 - 2_2$ line ($\nu_{\text{rest}} = 129.13892$ GHz) is close in frequency to SO₂ $J_{Ka,Kc} = 12_{1,11} - 11_{2,10}$ line ($\nu_{\text{rest}} = 129.10583$ GHz) and that contamination from the SO₂ $J_{Ka,Kc} = 12_{1,11} - 11_{2,10}$ line is therefore possible. The SO₂ $J_{Ka,Kc} = 10_{2,8} - 10_{1,9}$ ($\nu_{\text{rest}} = 129.51481$ GHz) and $J_{Ka,Kc} = 12_{2,10} - 12_{1,1}$ ($\nu_{\text{rest}} = 128.60513$ GHz) transitions at adjacent frequencies exhibit $\tau_{\text{max}} = 0.0060 \pm 0.0008$ and 0.0059 ± 0.0008 , respectively, while τ_{max} of SO $J_N = 3_3 - 2_2$ is 0.0214 ± 0.0012 (Kameno et al. 2020). Thus, the contamination of the SO₂ $J_{Ka,Kc} = 12_{1,11} - 11_{2,10}$ absorption would account for approximately 28%.

3 Results

3.1 Continuum nuclear emission

The 129 GHz continuum image of NGC 1052 is shown in figure 1. This is the first VLBI image at 129 GHz of the sub-pc scale continuum jet structure in this galaxy. A bright central source and a two-sided jet structure, with the eastern side approaching and the western side receding, extending over 8 mas (0.75 pc), are spatially resolved with the KVN synthesized beam. The jet appears to be well collimated. The bright central source is resolved into a bright component and the innermost jet components on both sides.

We identify five continuum components by performing two-dimensional Gaussian model fitting on the brightness distribution using the AIPS task JMFIT. These components are labeled as the eastern outer jet component (E1), the eastern innermost jet component (E2), the brightest component (Core), the western innermost jet component (W2), and the western outer jet component (W1), as shown in figure 1. The derived Gaussian fit parameters are summarized in table 1. The continuum components are aligned along a position angle of $64^\circ \pm 2^\circ$, which is in agreement with past VLBI observations at lower frequency bands (Jones et al. 1984; Kameno et al. 2001; Kadler et al. 2004).

3.2 SO $J_N = 3_3 - 2_2$ absorption

Spectral profiles of SO $J_N = 3_3 - 2_2$ absorption toward the continuum components (E1, E2, Core, W2, and W1) are presented in figure 2a–e. These profiles were extracted from the spectral cube by integrating over 0.3×0.3 mas² regions at each continuum component. The frequency resolution is 16 MHz, corresponding to a velocity resolution of 37.1 km s^{-1} . The typical rms noise per 16 MHz channel is 3 mJy beam^{-1} in the cube. SO absorption fea-

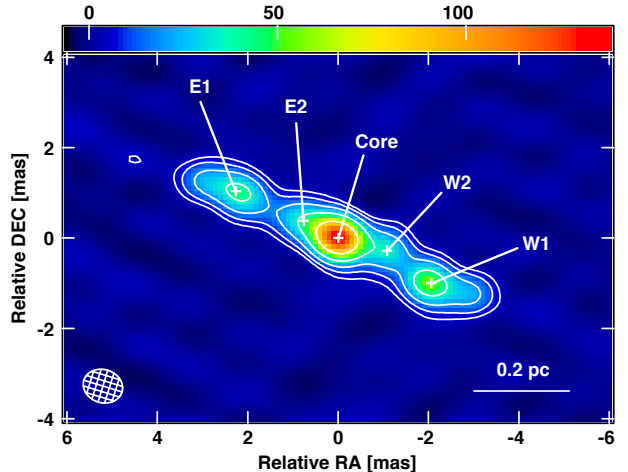


Fig. 1. Continuum map of the nuclear region in NGC 1052 at 129 GHz. Contours begin at 3 times I_{rms} and increase by a factor of 2, where $I_{\text{rms}} = 1.42 \text{ mJy beam}^{-1}$. The peak intensity is $125 \text{ mJy beam}^{-1}$. The synthesized beam is 0.88×0.73 mas at a PA of 73° as represented by a cross-hatched ellipse in the bottom-left corner. The plus symbols mark the location of fitted Gaussian components E1, E2, Core, W2 and W1. The parameters obtained from the Gaussian components are listed in table 1. Alt text: Contour map of the sub-pc region of NGC 1052 at 129 GHz, showing five labeled Gaussian components (E1, E2, Core, W2, and W1)

tures are clearly detected on the central components Core and W2, and marginally on the component E2 (figure 2b–2d). No significant absorption is found toward the jet components E1 and W1 (figure 2a and 2e).

Figure 3 displays the spectral profile of the SO absorption line integrated over three 0.3×0.3 mas² regions centered on the components E2, Core, and W2. The spectrum is binned to a velocity resolution of 55.6 km s^{-1} per channel, and all channels are normalized to the continuum level. Absorption features exceeding three times the rms noise (0.017 in normalized flux) are detected at the velocity channels of 1015, 1175, 1397, 1675 and 1731 km s⁻¹. The latter two redshifted channels (1675 and 1731 km s⁻¹) have velocities close to the HCN absorption peaks dominated by two redshifted components at 1656 and 1719 km s⁻¹ reported by Sawada-Satoh et al. (2016). The blueshifted feature at 1397 km s⁻¹ appears to correspond to the blueshifted component B1 identified in the 321 GHz H₂O maser emission by Kameno et al. (2024). The spectral profile reveals multiple velocity components, confirming both redshifted and blueshifted peaks around $V_{\text{sys}} + 200 \text{ km s}^{-1}$ and $V_{\text{sys}} - 120 \text{ km s}^{-1}$, as previously identified in the asymmetric profile with ALMA ($V_{\text{sys}} + 166 \text{ km s}^{-1}$ and $V_{\text{sys}} - 121 \text{ km s}^{-1}$; see figure 4 and table 3 in Kameno et al. 2023a).

In addition to the features described above, a further blueshifted absorption feature is detected at a velocity range of -500 to -300 km s⁻¹ relative to V_{sys} . The full SO absorption profile spans a broad velocity range of $> 700 \text{ km s}^{-1}$ (from 1015 to 1731 km s⁻¹). It can be decomposed into three distinct velocity groups, labeled Blue1, Blue2 and Red1 in figure 3. Blue1 and Red1 are prominent, with peak absorption depths exceeding 5% of the continuum level. This depth is larger than that seen in the ALMA data ($\sim 2\%$; Kameno et al. 2023a). The overall profile appears nearly symmetric around V_{sys} , in contrast to the asymmetric profile reported in the ALMA results.

A triple-Gaussian fit was applied to the spectrum, resulting in

Table 1. Parameters of continuum components by two dimension Gaussian fits

Component	S (mJy)	Δ R.A. (mas)	Δ Decl. (mas)	Major Axis (mas)	Minor Axis (mas)
(1)	(2)	(3)	(4)	(5)	(6)
E1	65 ± 3	$+2.26 \pm 0.02$	$+1.03 \pm 0.01$	1.52 ± 0.05	0.72 ± 0.02
E2	45 ± 3	$+0.76 \pm 0.02$	$+0.38 \pm 0.01$	1.19 ± 0.05	0.75 ± 0.03
Core	110 ± 2	0.00 ± 0.01	0.00 ± 0.01	0.87 ± 0.01	0.71 ± 0.01
W2	19 ± 2	-1.09 ± 0.02	-0.29 ± 0.02	0.94 ± 0.06	0.59 ± 0.04
W1	72 ± 3	-2.07 ± 0.02	-1.01 ± 0.01	1.37 ± 0.04	0.74 ± 0.02

Col.(1) Component ID, Col.(2) Flux density. Cols.(3)–(4) Relative position with respect to the phase center. Cols.(5)–(6) Full width at half maximum (FWHM) of the Gaussian component. Deconvolved major and minor axis sizes.

a χ^2 per degree of freedom = 36.8 / 29. The best-fit Gaussian components are overlaid on the spectrum in figure 3, and their parameters are listed in table 2. To assess the statistical significance of the fitted absorption components, we applied a *t*-test under the null hypothesis that the peak amplitude (A_p) is zero. The resulting *p*-values were less than 0.01 for all three components, confirming their statistical significant.

We examined whether Blue1 could be attributed to SO₂ 10_{2,8} – 10_{1,9} ($\nu_{\text{rest}} = 129.51481$ GHz) or SiO $J = 3 - 2, v = 1$ ($\nu_{\text{rest}} = 129.36335$ GHz). Kameno et al. (2023a) identified SO₂ 10_{2,8} – 10_{1,9} absorption at $V_{\text{sys}} + 161$ km s⁻¹ in the ALMA data. This absorption would appear at $V_{\text{sys}} - 712$ km s⁻¹, which differs by 300 km s⁻¹ from the velocity of Blue1 in figure 3. On the other hand, the SiO $J = 3 - 2, v = 1$ line would be located at $V_{\text{sys}} - 465$ km s⁻¹, which is within the velocity range of Blue1. However, no other SiO transitions have been found so far. Thus, we conclude that Blue 1 can be ascribed to blueshifted SO absorption.

Figure 4 illustrates the spatial distributions of SO optical depth in absorption, overlaid on the continuum contour map (figure 1). The maps reveal that SO absorption predominantly occurs toward the central continuum components, E2, Core, and W2. The SO optical depth distribution along the central components is asymmetric, with a pronounced enhancement toward the receding central component W2. In contrast, the outer jet components E1 and W1 exhibit little or no significant absorption at levels above three times the rms noise. The optical depth of SO measured with a high spatial resolution of < 0.1 pc achieved by the KVN is an order of magnitude higher than that from the ALMA observations by Kameno et al. (2023a).

4 Discussion

4.1 Continuum emission properties of the central source

The total 129 GHz continuum flux density of the central source (E2 + Core + W2) was measured to be 220 mJy in 2019. Assuming that the flux densities remained stable from 2017 to 2019, and using the 129 GHz flux density in 2019 together with the 89 GHz continuum flux density of the central component within 1.6 mas obtained in 2017 (414 mJy; Sawada-Satoh et al. 2019), we derive a steep spectral index $\alpha = -1.7$ ($S_{\nu} \propto \nu^{+\alpha}$) over the 89–129 GHz frequency range for the central source. As only two frequency data points are available, it remains uncertain whether the turnover frequency lies above or below 89 GHz. Nevertheless, we can conclude that the central source has an optically thin synchrotron spectrum at 129 GHz.

The lower limit of the brightness temperature (T_b) of the central source is estimated as $> 10^7$ K at 129 GHz, using the following

formula

$$T_b = 2 \ln 2 \frac{c^2 S_{\nu}}{\pi k_B r^2 \nu^2} (1 + z) \quad (1)$$

where c is the light speed, S_{ν} is the flux density at the frequency ν , k_B is the Boltzmann constant, r is the radius of the component and z is the redshift. The obtained T_b value supports the above argument that the detected continuum emission is dominated by non-thermal synchrotron emission.

4.2 SO absorption line profile and optical depth

As described in section 3.2, the SO $J_N = 3_3 - 2_2$ absorption in the KVN results is deeper than that of the ALMA data. The observed difference in depths may be mainly due to the different spatial resolution between the KVN (~ 0.7 mas, corresponding to 0.07 pc) and ALMA ($\sim 0.^{\prime\prime}3$, corresponding to 30 pc) observations. On sub-arcsecond scales with ALMA, the background continuum emission with the extended jets covers a region of several tens of parsecs, whereas the SO gas surrounding the SMBH is distributed within a much more compact region. Consequently, the covering factor of the gas becomes less than unity as the resolution becomes coarser.

Here we examine the effect of resolution on optical depth by estimating the intensity-weighted mean optical depth $\langle \tau \rangle$ and the mean covering factor $f_c = \langle \tau \rangle / \tau_{\text{max}}$ for the absorption components over the whole two-sided nuclear jet structure of the sub pc scale region (figure 4) in the same manner as that adopted by Sawada-Satoh et al. (2016) and Kameno et al. (2020). We estimate the mean optical depth $\langle \tau \rangle$ for each SO absorption feature, using

$$\langle \tau \rangle = \frac{\iint \tau(x, y) I(x, y) dx dy}{\iint I(x, y) dx dy}, \quad (2)$$

where $\tau(x, y)$ is the optical depth distribution of absorption feature shown in figure 4, and $I(x, y)$ is the 129-GHz continuum image shown in figure 1. The estimated $\langle \tau \rangle$ and f_c are listed in table 3, together with the SO $J_N = 3_3 - 2_2$ optical depth measured with a 30 pc spatial resolution by ALMA ($\tau_{30\text{pc}}$) from figure 3 in Kameno et al. (2023a). The derived mean covering factor f_c values are slightly lower than the covering factor yielded from the HCN $J = 3 - 2$ absorption (0.17; Kameno et al. 2023a). However, the values of $\langle \tau \rangle$ are at least three times higher than $\tau_{30\text{pc}}$. The discrepancy in optical depth can be attributed to differences in spatial resolution. Specifically, continuum emission from the extended jet of NGC 1052 is detected with ALMA but resolved out in the KVN data. Moreover, contamination from SO $J_N = 3_3 - 2_2$ emission may partially fill the absorption in the ALMA data, while the KVN spatially excludes such thermal contamination. It should be also noted that Kameno et al. (2023a) calculate the contamination-corrected SO $J_N = 3_3 - 2_2$ optical depth under the assumption that

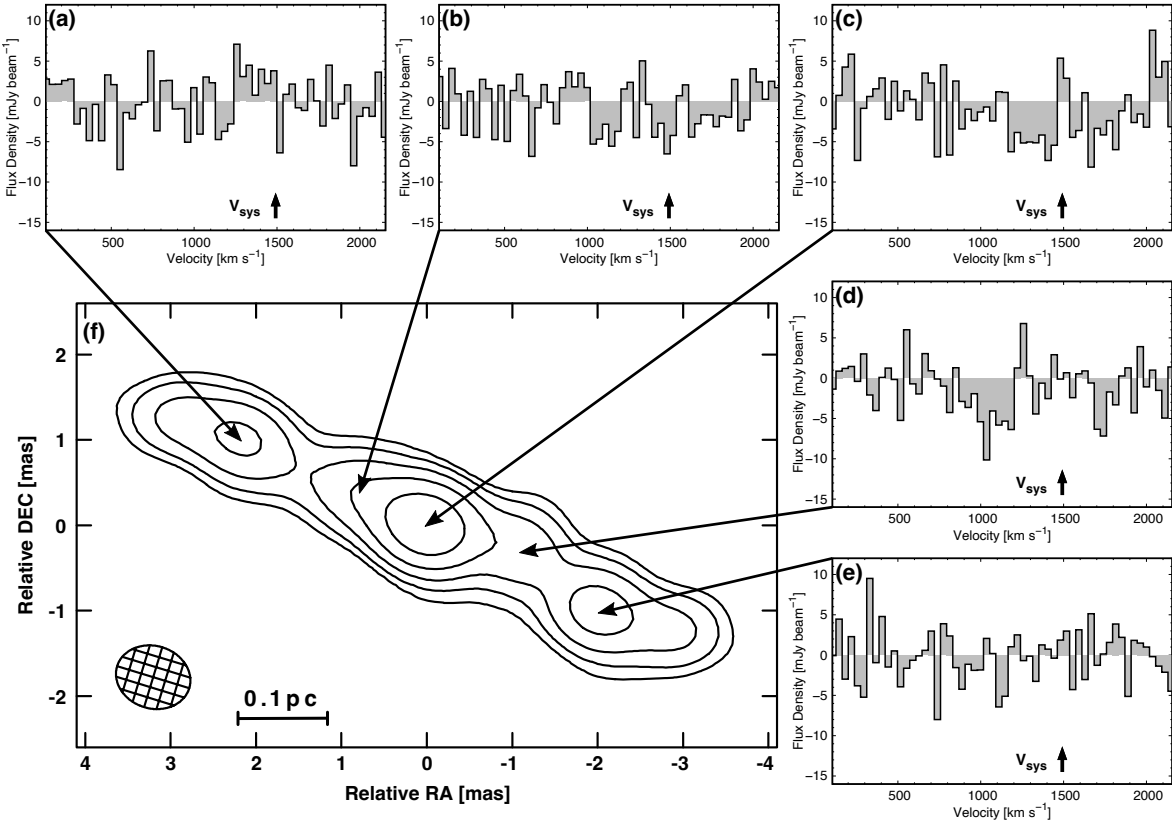


Fig. 2. (a)–(e) SO $J_N = 3_3 - 2_2$ absorption spectra integrated over a 0.3×0.3 mas 2 region at different locations of E1, E2, Core, W2 and W1, as marked by arrows. The zero flux level corresponds to the continuum level at each location. The velocity resolution is 37.1 km s $^{-1}$. (f) Continuum contour map of NGC 1052 at $\lambda 2$ mm also shown in figure 1. Alt text: Five panels showing SO line spectra at different locations (E1, E2, Core, W2, and W1), along with a continuum map of NGC 1052 indicating their spatial positions.

Table 2. Parameters of the SO $J_N = 3_3 - 2_2$ Gaussian line components

Absorption	A_p [*]	FWHM [†] (km s $^{-1}$)	V_{ctr} (km s $^{-1}$)	$V_{ctr} - V_{sys}$ (km s $^{-1}$)	t -test for A_p	
					t -value	p -value
Blue1	-0.057 ± 0.014	183 ± 22	1095 ± 22	-412	-4.21	0.000227
Blue2	-0.050 ± 0.018	80 ± 32	1392 ± 21	-115	-2.78	0.009444
Red1	-0.061 ± 0.014	173 ± 46	1730 ± 20	$+223$	-4.32	0.000166

* Peak amplitude of Gaussian component in normalized flux density.

† Full width at half depth in velocity.

|| Centroid velocity.

Table 3. SO $J_N = 3_3 - 2_2$ optical depth for each absorption component

Absorption (1)	τ_{max} (2)	$\langle \tau \rangle$ (3)	f_c (4)	τ_{30pc} (5)
Blue1	1.078	0.133	0.123	–
Blue2	0.593	0.065	0.110	0.010
Red1	0.508	0.075	0.147	0.021

Col.(1) Absorption ID. Col.(2) Maximum value of optical depth against W2. Col.(3) Mean optical depth. Col.(4) Mean covering factor. $f_c = \langle \tau \rangle / \tau_{max}$. Col.(5) Optical depth measured with a 30 pc spatial resolution by ALMA, from figure 3 in Kameno et al. (2023a).

the extra line equivalent width equals to the average of other SO₂ lines at 128.6 and 129.5 GHz, while the SO $J_N = 3_3 - 2_2$ optical depth derived from our KVN observations might be the result of possible blending with the SO₂ 12_{1,11} – 11_{2,10} line.

4.3 Location and kinematics of SO absorption

The absence of significant SO absorption against the outer jet components E1 and W1 places a spatial constraint on the distribution of the SO gas. The spatial extent of the SO gas must therefore be smaller than the angular separation between E1 and W1 (4.8 mas), which corresponds to an apparent size of less than 0.45 pc on the sky. The detection of absorption only toward the central source, and not toward the outer receding component W1, contrasts with the characteristics observed in the $\lambda 3$ mm HCN and HCO⁺ absorp-

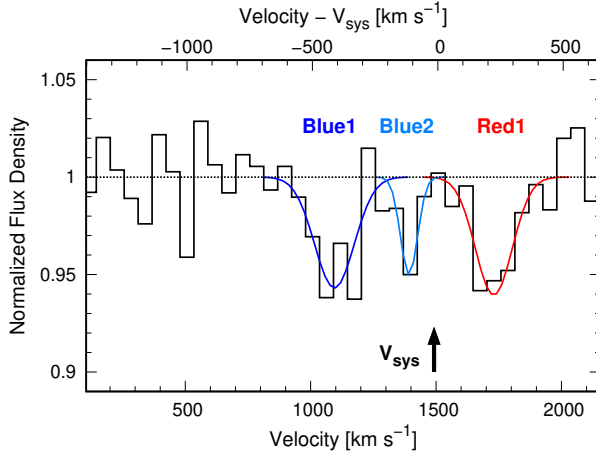


Fig. 3. Spectral profile of SO absorption integrated over three 0.3×0.3 mas 2 regions centered on the continuum components E2, Core, and W2. The spectrum is normalized by the combined continuum flux densities of E2, Core and W2. The velocity resolution is 55.6 km s $^{-1}$, and the rms noise level is 0.017 in normalized flux density. The three colored curves indicate a triple-Gaussian fit to the observed profile. The fitting results are listed in table 2. Alt text: A line graph displaying the SO absorption spectrum with three fitted components labeled Blue1, Blue2, and Red1.

tions (Sawada-Satoh et al. 2016, 2019). This concentration toward the central source is inconsistent with the SO gas being located in the molecular layer at the outer radii of the torus, where the HCN and HCO $^+$ gases lie. The enhanced SO optical depth of the central receding component W2 suggests that the SO gas resides at or close to the inner edge ($\ll 1$ pc) of the near side of the torus. The compact distribution of the high SO optical depth seen toward W2 at multiple velocities implies that small (< 0.1 pc) individual SO gas clumps are moving at various velocities across the line of sight to W2, which lies in the immediate vicinity of the SMBH. The variations in SO optical depth across the velocity channel maps (figure 4) highlight the inhomogeneous nature of the absorbing gas, supporting a clumpy gas structure. Since the velocity of the Red1 component is close to the peak velocities of 22 GHz H₂O maser emission and HCN $J = 1-0$ absorption, it is likely that Red1 arises from the ongoing infalling gas inside the torus towards the SMBH. This interpretation is in agreement with earlier results for the redshifted H₂O maser and HCN absorption features (Sawada-Satoh et al. 2008, 2016). On the other hand, Blue1 and Blue2 are the signature of at least two individual outward motions in the region.

The derived 129 GHz SO absorption spectrum and maps show partial similarities to the 321 GHz H₂O maser (Kameno et al. 2024) in terms of radial velocity and spatial distribution. In particular, several commonalities are observed between the Blue2 component of 129 GHz SO and the B1 component in the 321 GHz H₂O maser. First, the velocity of Blue2 in 129 GHz SO agrees well with that of the B1 component in the 321 GHz H₂O maser, though the entire velocity range of SO is much wider than that of H₂O. Second, both 129 GHz SO absorption and 321 GHz H₂O maser distributions extend westward along the jet direction for approximately 2 mas from the continuum peak position, where the SMBH is presumed to be located. The 321 GHz H₂O maser spots of B1 are predominantly distributed within 1 mas from the optically-thin continuum peak position. In the case of 129 GHz SO, Blue1, Blue2, and Red1 are all concentrated on W2. Among them, Blue2

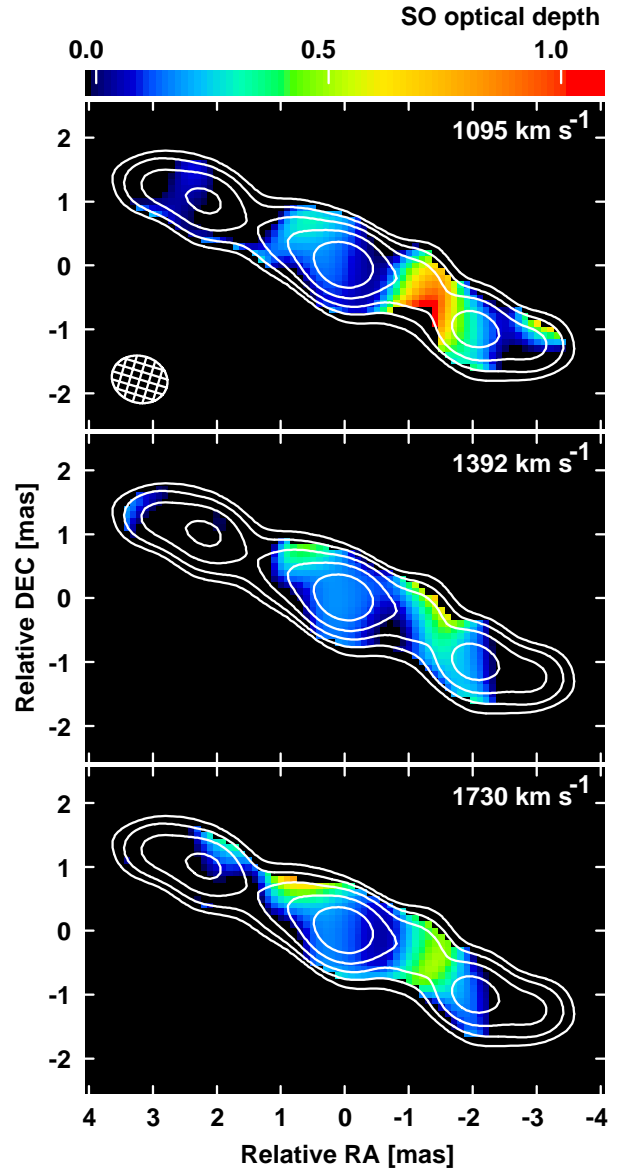


Fig. 4. Color optical depth channel maps of three SO absorption components. (Top) Blue1 at 1095 km s $^{-1}$, (Middle) Blue2 at 1392 km s $^{-1}$, (Bottom) Red1 at 1730 km s $^{-1}$. They are overlaid by the continuum contour map of NGC 1052 at $\lambda 2$ mm also shown in figure 1. The centroid velocity of each component is shown at the upper right. The rms noise in optical depth is typically 0.2. Alt text: Three color panels comparing the optical depth of different SO absorption components.

shows a somewhat prominent distribution that extends to Core as well, in contrast to Blue1 and Red1. This suggests that Blue2 of 129 GHz SO and B1 with its 321 GHz H₂O maser likely trace the same outward motion. Notably, however, no counterpart to the 129 GHz SO-Blue1 source is found in the 321 GHz H₂O maser line. The 129 GHz SO absorption is detected toward the millimeter jet components, while the 321 GHz H₂O maser is confined to a location in front of a compact sub-millimeter continuum source. Consequently, SO is more sensitive to the kinematic influence of the interaction region compared to H₂O, which could explain why the outflow traced by Blue1 is detectable only in SO. The spatial coincidence between 129 GHz SO absorption and the 321 GHz H₂O maser implies that the H₂O maser could be excited by the jet-torus interaction.

We have developed a plausible multiphase torus model (figure 5) that accounts for the observed characteristics of the SO absorption. At the innermost radii of the torus, the SO evaporation region is formed through shock heating resulting from the interaction between the sub-relativistic jets and torus gas, as suggested by Kameno et al. (2023a). The apparent size of the SO evaporation region is more compact than 0.45 pc. The evaporated SO molecular clumps are transported downstream by the jet, inducing an outflow. A fraction of the outflowing clumps subsequently falls back onto the equatorial plane of the torus and eventually infalls toward the SMBH through the torus. The infall velocity is considered to be approximately 200 km s⁻¹. The lines of sight to the central components intersect both outflowing and infalling clumps. Since the jet axis is slightly inclined relative to the sky plane, the near side of the torus should mainly obscure the SMBH and the receding jet side. The central receding component W2 exhibits a longer path length through the SO evaporation region along the line of sight compared to the approaching component E2. The difference in path length explains the high optical depth concentration observed toward W2. The model indicates that both outflow and infall coexist in a clumpy and dynamic structure within the sub-parsec region of NGC 1052, consistent with a clumpy dynamic torus (e.g., Wada et al. 2009; Kudoh et al. 2023).

NGC 1052 represents the first case in which sub-pc-scale jet-torus interactions, along with associated dynamical phenomena, such as inflows, outflows, and shock-induced molecular gas excitation, have been explored via sulfur-bearing molecular absorptions. Further applications of this observational approach to a broader AGN sample will contribute to a better understanding of the detailed physical processes governing jet-torus interactions and their impact on the circumnuclear environment.

5 Conclusions

We present the first sub-pc scale images of continuum and SO absorption in the center of NGC 1052 at 129 GHz using the KVN. The continuum image reveals a bright central source and symmetric two-sided jets extending 0.75 pc, with five distinct components (E1, E2, Core, W2, W1) identified. These components are aligned along a position angle of 64°, consistent with prior lower-frequency VLBI studies. The central source exhibits a steep spectral index ($\alpha = -1.7$) between 89 and 129 GHz, indicating optically thin synchrotron emission at 129 GHz. Its brightness temperature exceeds 10⁷ K, further supporting a non-thermal origin. SO absorption is clearly detected toward the central components Core, W2 and marginally at E2, with no significant absorption at E1 and W1. The absorption profile spans a broad velocity range over 700 km s⁻¹, showing three distinct velocity groups. The SO absorp-

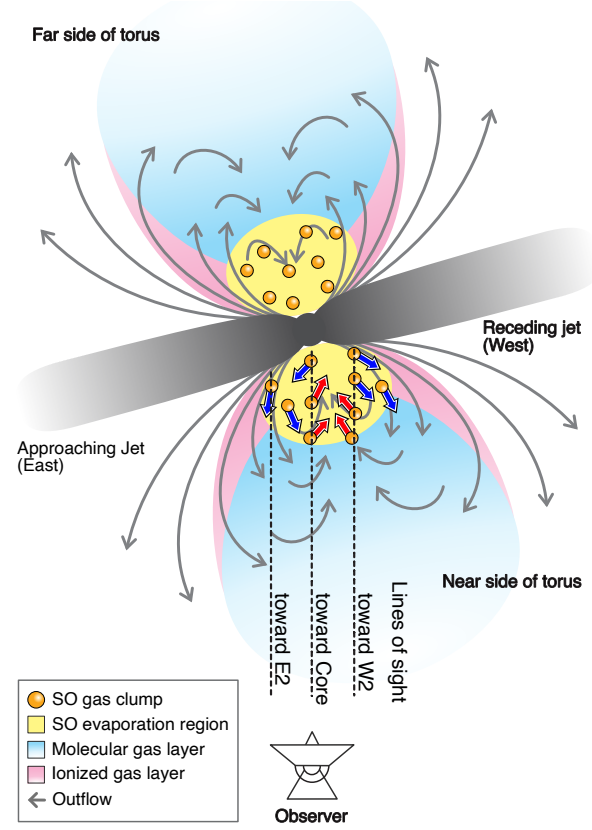


Fig. 5. A schematic view of the sub-pc nuclear region in NGC 1052. The two-sided jet axis is inclined by $\geq 76^\circ$ with respect to the line of sight (Sawada-Satoh et al. 2008). The torus has several phase layers of plasma and molecules. Shock heating caused by interactions between sub-relativistic jets and torus gas generates a compact SO evaporation region, smaller than 0.45 pc. Clumps containing evaporated SO are carried outward by the jet, forming outflows (blue arrows). Some of the clumps fall back onto the equatorial plane and eventually infall toward the SMBH (red arrows). The longer line-of-sight path through the SO-rich region toward the central receding component explains its high optical depth. Alt text: A cartoon showing the possible environment in the torus and jets in NGC 1052.

tion is concentrated toward the central components, with a pronounced enhancement at the receding W2 component. The spatial distribution of SO absorption indicates the absorbing gas is concentrated within a region smaller than 0.45 pc, likely located close to the inner edge of the torus. The distribution and velocity structure of SO absorption suggest that the SO gas forms clumpy and small-scale (< 0.1 pc) structures, showing both inflow and outflow motions. To explain the spatial and kinematic properties of the SO absorption, we propose a multiphase torus model in which jet-torus interactions produce shock-heated regions at the inner edge of the torus, leading to SO gas evaporation and the formation of SO clumps. These clumps are entrained by the jet and transported outward, while some clumps fall back toward the SMBH, creating inflow signatures. The line of sight intersects both outflowing and infalling clumps, producing the observed absorption profile and velocity structure. Our observations also reveal that the 129 GHz SO absorption shows partial similarities to the 321 GHz H₂O maser in both radial velocity and spatial distribution. The spatial coincidence between SO absorption and H₂O maser emission suggests that the excitation of the H₂O maser could be linked to the

jet–torus interaction.

Acknowledgments

We are grateful for the excellent support provided by the staff of the KVN. The KVN and a high-performance computing cluster are facilities operated by the KASI (Korea Astronomy and Space Science Institute). The KVN observations and correlations are supported through the high-speed network connections among the KVN sites provided by the KREONET (Korea Research Environment Open NETwork), which is managed and operated by the KISTI (Korea Institute of Science and Technology Information). This research was partially supported by JSPS KAKENHI grant No. 21K03628.

References

Antonucci, R. 1993, *ARA&A*, 31, 473.

Asada, K. & Nakamura, M. 2012, *ApJL*, 745, L28.

Baczko, A.-K., Schulz, R., Kadler, M., et al. 2016, *A&A*, 593, A47.

Baczko, A.-K., Ros, E., Kadler, M., et al. 2022, *A&A*, 658, A119.

Baloković, M., Cabral, S. E., Brenneman, L., et al. 2021, *ApJ*, 916, 2, 90.

Barth, A. J., Filippenko, A. V., & Moran, E. C. 1999, *ApJL*, 515, 2, L61.

Claussen, M. J., Diamond, P. J., Braatz, J. A., et al. 1998, *ApJL*, 500, L129.

Deller, A. T., Tingay, S. J., Bailes, M., et al. 2007, *PASP*, 119, 318.

Fromm, C. M., Younsi, Z., Baczko, A., et al. 2019, *A&A*, 629, A4.

Gabel, J. R., Bruhweiler, F. C., Crenshaw, D. M., et al. 2000, *ApJ*, 532, 883.

Greisen, E. W. 2003, *Information Handling in Astronomy - Historical Vistas*, 285, 109.

Hada, K., Kino, M., Doi, A., et al. 2013, *ApJ*, 775, 70.

Han, S.-T., Lee, J.-W., Kang, J., et al. 2008, *International Journal of Infrared and Millimeter Waves*, 29, 69.

Han, S.-T., Lee, J.-W., Kang, J., et al. 2013, *PASP*, 125, 539.

Impellizzeri, V., Roy, A. L., & Henkel, C. 2008, *The role of VLBI in the Golden Age for Radio Astronomy*, 9, 33.

Kadler, M., Ros, E., Lobanov, A. P., et al. 2004, *A&A*, 426, 481.

Kameno, S., Sawada-Satoh, S., Inoue, M., et al. 2001, *PASJ*, 53, 169.

Kameno, S., Inoue, M., Wajima, K., et al. 2003, *PASA*, 20, 134.

Kameno, S., Nakai, N., Sawada-Satoh, S., et al. 2005, *ApJ*, 620, 145.

Kameno, S., Sawada-Satoh, S., Impellizzeri, C. M. V., et al. 2020, *ApJ*, 895, 73.

Kameno, S., Sawada-Satoh, S., Impellizzeri, C. M. V., et al. 2023a, *ApJ*, 944, 156.

Kameno, S., Harikane, Y., Sawada-Satoh, S., et al. 2023b, *PASJ*, 75, L1.

Kameno, S., Harikane, Y., Sawada-Satoh, S., et al. 2024, *PASJ*, 76, 340.

Kellermann, K. I., Vermeulen, R. C., Zensus, J. A., et al. 1998, *AJ*, 115, 1295.

Kemball, A. J., Diamond, P. J., & Cotton, W. D. 1995, *A&AS*, 110, 383

Kudoh, Y., Wada, K., Kawakatu, N., et al. 2023, *ApJ*, 950, 1, 72.

Jones, D. L., Wrobel, J. M., & Shaffer, D. B. 1984, *ApJ*, 276, 480.

Lee, S.-S., Oh, C. S., Roh, D.-G., et al. 2015, *Journal of Korean Astronomical Society*, 48, 125.

Liszt, H. & Lucas, R. 2004, *A&A*, 428, 445.

Lynden-Bell, D. 1969, *Nature*, 223, 690.

Middelberg, E., Roy, A. L., Walker, R. C., et al. 2005, *A&A*, 433, 897.

Nakahara, S., Doi, A., Murata, Y., et al. 2020, *AJ*, 159, 14.

Omar, A., Anantharamaiah, K. R., Rupen, M., et al. 2002, *A&A*, 381, L29.

Oyama, T., Kono, Y., Suzuki, S., et al. 2016, *PASJ*, 68, 105.

Oyama, T., Nagayama, T., Yamauchi, A., et al. 2024, *PASJ*.

Pineau des Forets, G., Roueff, E., Schilke, P., et al. 1993, *MNRAS*, 262, 915.

Rioja, M. & Dodson, R. 2011, *AJ*, 141, 114.

Sawada-Satoh, S., Kameno, S., Nakamura, K., et al. 2008, *ApJ*, 680, 191.

Sawada-Satoh, S., Roh, D.-G., Oh, S.-J., et al. 2016, *ApJL*, 830, L3.

Sawada-Satoh, S., Byun, D.-Y., Lee, S.-S., et al. 2019, *ApJL*, 872, L21.

Ulvestad, J. S., Antonucci, R. R. J., & Barvainis, R. 2005, *ApJ*, 621, 123.

Urry, C. M. & Padovani, P. 1995, *PASP*, 107, 803.

Vermeulen, R. C., Ros, E., Kellermann, K. I., et al. 2003, *A&A*, 401, 113.

Wada, K., Papadopoulos, P. P., & Spaans, M. 2009, *ApJ*, 702, 1, 63.

Woo, J.-H. & Urry, C. M. 2002, *ApJ*, 579, 2, 530.

Wrobel, J. M. 1984, *ApJ*, 284, 531.